SEARCH FOR $z \sim 7$ Lyα EMITTERS WITH THE SUPRIME-CAM AT THE SUBARU TELESCOPE

P. HIBON[1,2], N. KASHIKAWA[3,4], C. WILLOTT[5], M. IYE[3,4], AND T. SHIBUYA[3,4]

[1] Gemini Observatory, La Serena, Chile; phibon@gemini.edu
[2] School of Earth and Space Exploration, Arizona State University, Tempe, AZ 85287, USA
[3] Optical and Infrared Astronomy Division, National Astronomical Observatory, Mitaka, Tokyo 181-8588, Japan
[4] Department of Astronomy, School of Science, Graduate University for Advanced Studies, Mitaka, Tokyo 181-8588, Japan
[5] Herzberg Institute of Astrophysics, National Research Council, Victoria, BC V9E 2E7, Canada

ABSTRACT

We report a search for $z = 7$ Lyα emitters (LAEs) using a custom-made narrowband filter centered at 9755 Å with the Suprime-Cam instrument installed at the Subaru telescope. We observed two different fields and obtained two samples of seven LAEs, of which four are robust in each field. We cover the luminosity range of 9.10^{42}–2.10^{43} erg s^{-1} in comoving volumes of $\sim 4 \times 10^5$ and 4.3×10^5 Mpc^3. From this result, we derived possible $z \sim 7$ Lyα luminosity functions for the full samples and for a subsample of four objects in each field. We do not observe, in each case, any strong evolution between the $z = 6.5$ and $z \sim 7$ Lyα luminosity functions. Spectroscopic confirmation for these candidate samples is required to establish a definitive measure of the luminosity function at $z \sim 7$.

Key words: early universe – galaxies: distances and redshifts – galaxies: high-redshift – galaxies: luminosity function, mass function

Online-only material: color figures

1. INTRODUCTION

Galaxies formed at high redshifts play a key role in understanding how and when the reionization of the universe took place. They also help constrain the physical mechanisms that drove the formation of the first stars and galaxies in the universe. Over the last decade, the limits of the observable universe have been pushed to $z \sim 6$, which corresponds to $\sim 90\%$ of the age of the universe. The detection of galaxies formed at high redshifts will allow us to probe the era of reionization. Selecting galaxies with strong emission lines, such as Lyα lines, allows us to probe the high-redshift Lyα luminosity function (LF).

The search for the redshifted Lyα emission at the longest possible wavelength is complicated by the presence of OH emission lines within the terrestrial atmosphere. This strong emission line is responsible for the faintness limit at which celestial objects can be detected with ground-based telescopes at near-infrared (NIR) wavelengths. Fortunately, there are spectral intervals with a lower OH background that allow for a fainter detection limit from the ground-based observations. This is known as the narrowband (NB) imaging technique. This is one of the most successful methods for detecting strong Lyα emission lines of galaxies since it relies on a specific redshift interval as well as a selected low-sky background window. This filter allows for maximum detection of light from the Lyα emitters (LAEs) at the central wavelength, while minimizing the adverse influences of sky emission.

Over 100 $z > 6$ LAEs have been photometrically selected and spectroscopically identified in this way since Hu et al. (2002). Kashikawa et al. (2011) obtained an exhaustive sample of LAEs (45 at $z = 6.5$ and 54 at $z = 5.7$ spectroscopically confirmed) from which a first robust estimate of the Lyα LF was derived. This LF shows an apparent deficit compared to the $z = 5.7$ Lyα LF of Shimasaku et al. (2006), corresponding to possible luminosity evolution from $z = 5.7$ to $z = 6.5$ of $L^*_{z=6.6} \sim 0.4$–$0.6 \, L^*_{z=5.7}$. They concluded that the reionization of the universe has not been completed at 6.5.

Ouchi et al. (2010) have obtained the largest sample to date: 207 LAEs at $z = 6.6$ with the NB imaging technique. Their derived $z = 6.6$ apparent Lyα LF indicates a decrease from 5.7 at the 90% confidence level with a more dominant decrease of luminosity evolution (L^*) than of number evolution (Φ^*), in agreement with Kashikawa et al. (2006). They therefore claim that the hydrogen in the intergalactic medium (IGM) is not highly neutral at $z = 6.6$.

Hu et al. (2010) obtained 88 $z \sim 5.7$ and 30 $z \sim 6.5$ LAEs. Their results on the evolution of the Lyα LF are in agreement with previous works from Malhotra & Rhoads (2004) and Kashikawa et al. (2006).

Iye et al. (2006) first spectroscopically confirmed a $z = 6.96$ LAE. From this result, Ota et al. (2008) assumed an evolution of density from $z = 5.7$ to $z \sim 7$. They found that the IGM is not highly neutral at $z \sim 7$ and the neutral hydrogen fraction could evolve from $x_{\rm H\,I}^{z=6.6} \sim 0.24$–$0.36$ to $x_{\rm H\,I}^{z \sim 7} \sim 0.32$–$0.64$. Hibon et al. (2011) also performed a search for $z \sim 7$ LAEs using the IMACS instrument at the Magellan telescope. This study resulted in a sample of six $z \sim 7$ LAEs candidates, for which the spectroscopic follow-up data are in analysis.

We present here a new NB imaging survey with the Suprime-Cam/Subaru telescope—targeting $z \sim 7$ LAEs with the custom-made $NB973$ filter ($\lambda_{\rm center} = 9755$ Å, FWHM = 200 Å). This paper first presents the data (Section 1) and the data reduction procedure (Section 2). We then describe the method of selection and contamination of low-redshift interlopers for high-redshift LAEs in Section 3. We present the final sample of $z \sim 7$ LAEs and Lyα LF at this redshift in Section 4.

Throughout this study, we adopt the following cosmological parameters: $H_0 = 70$ km s^{-1} Mpc^{-1}, $\Omega_m = 0.3$, and $\Omega_\Lambda = 0.7$ (Spergel et al. 2007). All magnitudes are AB magnitudes.

2. OBSERVATIONS AND DATA REDUCTION

2.1. Observations

The data were taken with the Suprime-Cam instrument (the Subaru Prime Focus Camera), installed at the 8 m Subaru

Table 1
Observational Data

Instrument	Band	Integration Time (hr)		Limiting Magnitudes[a]	
		D33	D41	D33	D41
MegaCam	u^*	21.3	21.4	27.5	27.4
MegaCam	g'	22.1	24.4	27.5	27.2
MegaCam	r'	39.6	40.7	27.0	26.8
MegaCam	i'	69.3	65	26.6	26.5
MegaCam	z'	48.7	44.5	25.5	25.4
Suprime-Cam	$NB973$	5	6.3	24.3	24.7
WIRCam	J	4.6	4.8	24.5	24.4
WIRCam	H	4.4	4.1	24.4	24.1
WIRCam	$K_{\rm s}$	4.8	3.9	24.2	24.3

Note. [a] 5σ magnitude limits in apertures $2''$ in diameter for MegaCam, WIRCam, and Suprime-Cam.

telescope at the National Astronomy Observatory of Japan. This instrument delivers a mosaic of 10 2048×4096 CCDs, which covers a $34' \times 27'$ field of view with a pixel scale of $0\rlap{.}''20$. A new CCD, with a quantum efficiency two times better than the preceding one at the red end ($\lambda = 8000$–$10400\,\text{Å}$), was installed.

By taking exposures lasting 20 minutes, we ensured background-limited performance. We did offset the telescope between each exposure. The offset sequence for each field and night was chosen randomly.

We targeted two fields (hereafter called D33 and D41) covered by the Canada–France–Hawaii Telescope Legacy Survey (CFHT-LS) and the WIRCam Deep Survey (WIRDS; PIs: C. Willott and J.-P. Kneib).[6] The total area of the survey, the two fields considered, is 2340 arcmin^2.

We observed using the custom-made NB filter centered at 9755 Å with a wavelength range of $\Delta\lambda = 200\,\text{Å}$ ($NB973$) during two nights in 2009 July. During these observations, the conditions were partially good: we obtained 15 and 19–20 minute exposures during these nights with a seeing varying between $0\rlap{.}''5$ and $0\rlap{.}''85$.

The total exposure time for each epoch of data is given in Table 1.

2.2. NB Data Reduction

Using the Data Reduction Software developed for the Subaru Suprime-Cam instrument (Ouchi et al. 2004; Yagi et al. 2002), we perform the following steps: a bias subtraction, a flat fielding, a distortion and atmospheric dispersion correction, a sky subtraction, a bad region masking of elements such as satellite trails and an acquisition and guiding probe, the alignment of the individual exposures, and the final co-adding step resulting in a stacked image. After eliminating the low signal-to-noise regions at the edges of the field of view, we obtain an effective area of 1118 arcmin^2 for the D33 field and 1202 arcmin^2 for the D41 field.

We realize the astrometric calibration on the individual images before the final stacking using the UCAC2 catalog (Zacharias et al. 2004).

We then need to adjust the World Coordinate System parameters to obtain a more precise alignment. For this purpose we use the IRAF task *msctpeak* to interactively align the catalog stars in our images and update their headers. We finally obtain an astrometry calibration for each individual image with a precision of rms $\sim \pm 0.1$ arcsec in both directions.

The photometric calibration of the u^*, g', r', i', z' broadband CFHT-LS data (described in the next section) is based on the Sloan Digital Sky Survey (SDSS) data for stars with $17 < i' < 21$ and the MegaCam–SDSS color transformation equations of Regnault et al. (2009). The precision obtained in u^*, g', r', i', z' is between 0.03 and 0.02 mag. As the $NB973$ filter is included in the z'-band filter, we calibrate our $NB973$-stacked images using the AUTO magnitude from the z'-band SExtractor catalog. We perform the calibration on 1500 non-saturated stars within $16 < z' < 20$. Considering the photometric error on the broadband calibration, we obtain a photometric calibration precisely at 0.1 mag in $NB973$.

To estimate the limiting magnitude for the different bands, we use the script *limitmag.cl* available in the SDFRED package. This task constructs a count distribution from random photometric apertures on the image. Then it fits a Gaussian profile into this distribution, obtains the sigma number of this profile, and calculates the limiting magnitude of the image. We report in Table 1 the limiting magnitude for each band in each field.

2.3. Broadband Data

Very deep optical imaging data of our observed fields are available through the CFHT-LS. For the purpose of this study, we make use of the T0006 release. These data products are available from the CADC archive and take the form of image stacks in the u^*, g', r', i', z' filters and of ancillary data such as weight maps, catalogs, etc. The spectral curves of the filters u^*, g', r', i', z' are similar to those of SDSS filters. We also have in hand the Near-Infrared Deep Imaging data from the WIRDS (PIs: C. Willott and J.-P. Kneib; R. Bielby et al. in preparation).

These optical data have been calibrated photometrically using the SDSS photometry, and the NIR data have been calibrated using the 2MASS photometry (McCracken et al. 2010). Considering internal and external photometric error sources, the uncertainty on the optical and the NIR data photometry is ~0.03 mag and ~0.02 mag, respectively.

As the broadband data and the NB data do not have the same pixel scale, we resample the broadband data using the software SWARP to obtain optical and NIR images with 0.2 arcsec pixel^{-1}. The alignment in pixels is then verified using IRAF *geomap*/*geotran* tasks.

Our complete set of data is therefore scaled at 0.2 arcsec pixel^{-1} and covers an effective area of 1118 and 1202 arcminutes^2, for D33 and D41 fields, respectively.

A summary of the observational data for both fields, D33 and D41, used in this paper is provided in Table 1. Figure 1 shows the transmission curves of the filters corresponding to the multi-band data used in this study.

3. SAMPLE

3.1. Catalog Generation

We generate the catalogs using the software SExtractor of Bertin & Arnouts (1996). We use the dual-image mode: the first
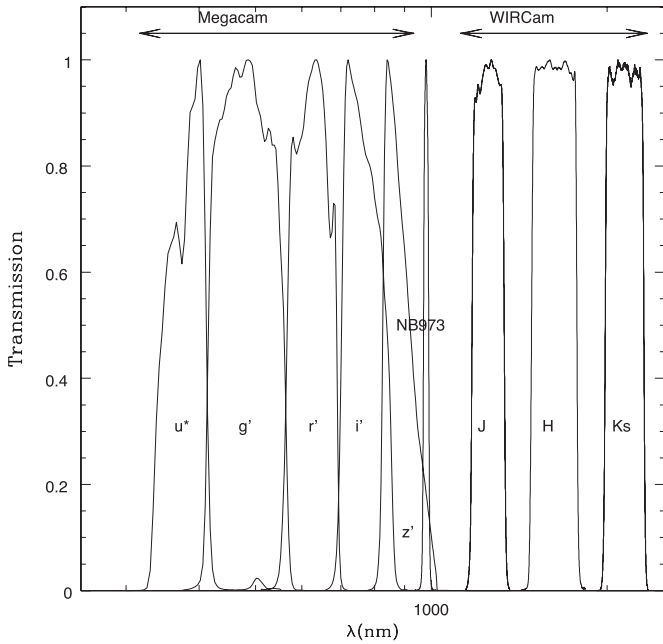
Figure 1. Transmission curves of the filters corresponding to the complete set of data used in this paper. All transmissions are normalized to 100% at maximum.

image, the detection image, has been set as the combined $NB973$ image; the second image, the measurement image, corresponds to the resampled images from the optical and NIR bands.

We choose to detect objects in 7 pixels above a threshold of 1.2σ. The aperture used for the photometry is $1''$.

3.2. Selection

Criterion 1: SNR($NB973_{\rm combined}$) $> 5\sigma$. We selected objects with a 5σ detection on the combined $NB973$ images.

Criterion 2: SNR(u^*, g', r', i', χ^2) $< 3\sigma$. Due to the Gunn–Peterson trough, i.e., the nearly complete absorption of the flux shortward of Lyα as a result of the large neutral hydrogen column density in the IGM, we observe spectral discontinuity at redshifts greater than about 6. We are therefore searching for objects that are not detectable in optical (u^*, g', r', i') bands. A possible method, therefore, is to select objects with less than a 3σ detection in filters blueward of the expected Lyα emission: u^*, g', r', i'.

The color break between the optical and $NB973$ filters is high and covers a wide spectral range. Moreover, for the CFHT-LS, the Terapix data center generated a deep χ^2 image combining the g', r', and i' images. We consider therefore this χ^2 image as well as the other blueward optical filters, and we select objects with less than a 3σ detection in the χ^2 image.

In summary, we select objects with less than a 3σ detection in the u^*, g', r', i', and χ^2 bands.

Criterion 3: a color criterion between z' and $NB973$ data. The $NB973$ filter used for this study is included in the broad z-band filter. Although we expect an excess of flux in $NB973$, it is still possible to observe part of the continuum in the z-band filter. From Criterion 1 and Criterion 2, we can define the following color criterion: $z' - NB973 > 0.65$ mag. We use the same $NB973$ filter as Ota et al. (2008) have used for the search of robust $z = 7$ LAEs in the Subaru Deep Field. Their search was successful, as it resulted in the spectroscopic confirmation of the only $z \sim 6.96$ spectroscopically confirmed LAE. Following the simulation they performed and plot in their

Figure 3, we also check the color $z' - NB973$ of our candidates with a second color criterion: $z' - NB973 > 1.72$ mag. We show our candidates in Figure 2, representing $z' - NB973$ versus $NB973$ for both fields, and the two color criteria. The points answering $z' - NB973 > 0.65$ mag but not $z' - NB973 > 1.72$ mag are the points with no z'-band detection. We then use the 3σ limit of the z'-band data for these objects.

Criterion 4. $NB973 - J < 0$, $NB973 - H < 0$, and $NB973 - Ks < 0$.

To avoid some contamination by low-redshift objects, we choose to set NIR criteria. More explanations are given in Section 3.3.

Criterion 5. High-redshift objects are identified as compact point-like sources. After carefully applying all the criteria presented above, we visually inspect each candidate to confirm their point-like source aspects. Objects with a different aspect are more likely artifacts. For D33 7 out of 9 objects and for D41 7 out of 10 objects are selected as serious candidates.

3.3. Contaminants

3.3.1. Transient Objects

Since the NB and broadband data were taken at different times, it is possible for transient objects to appear in one filter and not another. Transient objects that are brighter than the NB detection limit will be considered as candidates if they are not visible in the broadband images.

Kulkarni & Rau (2006) used a transient rate for supernovae (SNe), including Type Ia, b, c, and Type II, of 5×10^4 Gpc^3 yr^{-1}. From Cappellaro et al. (1999), we know that the transient rate of Type Ia SNe is approximately a factor of 3.4 lower than the transient rate including Type Ia, b, c, and Type II SNe. Therefore, by applying a transient rate of $5 \times 10^4/3$ to each of our fields, we can estimate that 0.8 Type Ia SNe could be detected in the D33 field and 0.9 Type Ia SNe in the D41 field.

We also choose to estimate the number of SNe that we could have detected in our survey using the method of Ota et al. (2008). We assume the same mean object color as Ota et al. (2008) did, $i' - NB973 = 0.33$, and use the results of variability. For their large magnitude variation (1.1–1.6 mag), Ota et al. (2008) found one object at each epoch giving $P \sim 10^{-5}$. Down to $i' \sim 26.5$, we find approximately 7500 objects in D33 and 9000 objects in D41. From this method, we obtain an estimated number of variable objects of ~ 0.75 object for D33 and ~ 0.9 object for D41.

In summary, both methods seem to agree on a possible contamination of one transient object per field.

3.3.2. L–T Dwarfs

Considering Figure 9 of Hawley et al. (2002), which presents several color diagrams for L- and T-dwarfs detected in SDSS, we know that M-, L-, and T-dwarfs have $z' - J > 1$ and L-, T-dwarfs have $z' - J > 2$. Therefore, although our J band is shallower than our $NB973$ limiting magnitude, the criterion $NB973 - J < 0$ still secures non-contamination of our LAE sample by L- and T-dwarfs. We therefore avoid selecting L- and T-dwarfs.

3.3.3. Foreground Emitters

We estimate that the lower value on equivalent width that a line emitter, with a flat continuum in f_ν, will have if selected with our criteria using the formula from Rhoads & Malhotra
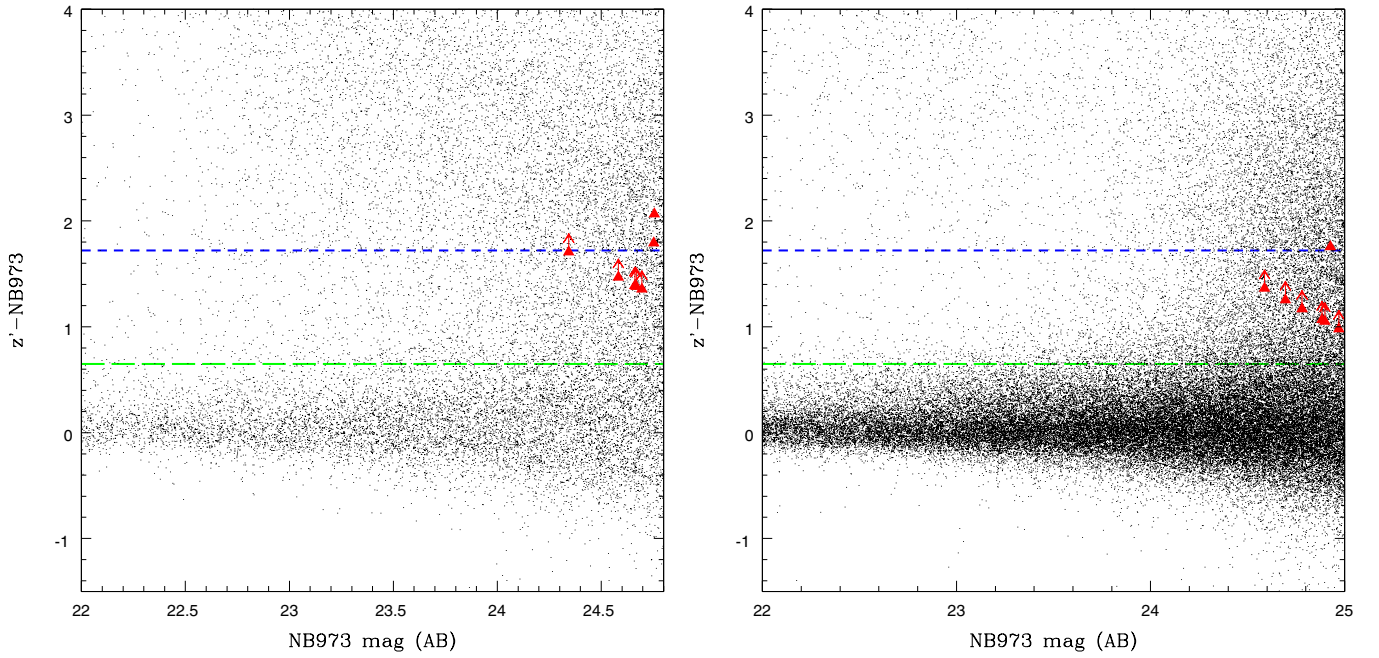
Figure 2. Color–magnitude diagram $z' - NB973$ vs. $NB973$ for the D33 field (left) and the D41 field (right), showing the candidates (red triangles) obtained with the criterion $z' - NB973 > 0.65$ mag (green dashed line). We also compare them to the criterion $z' - NB973 > 1.72$ mag (blue short dashed line). The black dots represent all the objects present in each field with $SNR(NB973_{combined}) > 5\sigma$.

(A color version of this figure is available in the online journal.)

(2001) will require:

$$\mathrm{EW}_{\min} \sim \left(\frac{f_{NB}}{f_{BB}}\right) \Delta\lambda_{NB} = \left[\frac{5\sigma_{NB}}{3\sigma BB} - 1\right] \Delta\lambda_{NB}, \qquad (1)$$

with f_{NB} and f_{BB} being the flux in $NB973$ and the g' band, respectively, $\Delta\lambda_{NB}$ the width of the $NB973$ filter, and σ_{NB} and σ_{BB} the flux uncertainties in $NB973$ and the g' band, respectively. We therefore obtained $\mathrm{EW}_{\min}^{D33} \sim 840$ Å and $\mathrm{EW}_{\min}^{D41} \sim 714.2$ Å. Foreground line emitters would then require an equivalent width $\mathrm{EW}_{\min}^{D33} \geqslant 840$ Å and $\mathrm{EW}_{\min}^{D41} \geqslant 714.2$ Å to contaminate our Lyα selection sample.

1. *Hα at z ∼ 0.47.* Salzer et al. (2005) presented the typical equivalent width of low-redshift galaxies. They found that Hα emitters at $z \sim 0.4$ have EW < 200 Å. From Equation (1), the lower limit on the Hα emitter equivalent width in our survey is 840 Å in the D33 field and 714.2 Å in the D41 field. Hα emitters at $z \sim 0.47$ can therefore not contaminate our candidate selection.

2. *[O III] at z ∼ 0.95.* Xia et al. (2011) studied the line emitters in the PEARS survey and observed that [O III] emitters at $z \sim 1$ generally have an equivalent width lower than 500 Å. Moreover, looking at the typical spectral energy distributions of [O III] emitters at $z \sim 0.9$, we remark that these foreground emitters are brighter in the Ks band than in the J band and with typical J band magnitude ~ 23 (AB). We will have therefore observed these objects in our very deep NIR data. Considering the lower limit on equivalent width that line emitters will have to contaminate our candidate sample and the NIR magnitudes of typical $z \sim 0.9$–1 [O III] emitters, the contamination by these foreground emitters is therefore ruled out.

   Cardamone et al. (2009) found low-redshift [O III] emitters with very high observed EWs, reaching values up to

1500 Å. However, these emitters have very bright magnitudes in optical bands: $18 \leqslant g', r', i', z' \leqslant 21$ and blue spectra. They would therefore be easily detected by the CFHT-LS data. These emitters are identified as Pea galaxies: luminous blue compact galaxies.

3. *[O II] at z ∼ 1.6.* Hayashi et al. (2011) studied [O II] emitters at $z \sim 1.46$. Figure 8 of Hayashi et al. (2011) shows these emitters in a color–magnitude diagram $z' - K_s$ versus K_s. $z \sim 1.46$ [O II] emitters have $K_s \in [20; 23]$, and $z' - K_s > 0$. As our NB filter is included in the z'-band filter, as seen in Figure 1, we can assume that $z' - K_s > 0$. This color does not agree with our Criterion 4. Figure 10 of Hayashi et al. (2011) shows the color–color diagram $z' - K_s$ versus $J - K_s$. Most of their [O II] emitters have not only a $z' - K_s > 0$ but also a $J - K_s > 0$. In the case of our sample, a deeper J-band image would help us eliminate the [O II] emitters as a possible contaminant to verify that our candidates have $J - K_s < 0$, as deduced from Criterion 4.

   However, our K_s-band data do not entirely cover both fields. Although the contamination by $z \sim 1.6$ [O II] emitters is very unlikely due to the K_s magnitude range, we cannot completely rule it out.

3.3.4. Red Continuum Galaxies

1. *Balmer break galaxies.* Balmer break galaxies at $z \sim 1.4$ also need to be considered as a possible contamination source. However, from Figure 4 of Delorme et al. (2010), we obtain an estimation of the color $z' - J$ for $z \sim 2$ Balmer break galaxies: $z' - J > 0$. Daddi et al. (2004) showed that $z \geqslant 1.4$ Balmer break galaxies have $z' - K_s > 1.5$. Moreover, in the case of continuum objects, we can assume that $z' - Ks \sim NB973 - Ks$. During the selection of our candidate sample, we applied Criterion 4: $z' - J < 0$. If

4

Table 2
The $z \sim 6.96$ LAE Candidates for the D33 Field

Name	NB973	Error	SNR(NB973)	z'	Error	SNR(z')	EW[a] (Å)
LAE 1	24.3	0.17	7.7	>25.46	⋯	⋯	>24
LAE 2	24.6	0.2	6.1	>25.46	⋯	⋯	>24.3
LAE 3	24.7	0.21	5.7	>25.46	⋯	⋯	>24.3
LAE 4	24.7	0.21	5.6	>25.46	⋯	⋯	>24.3
LAE 5	24.7	0.22	5.5	>25.46	⋯	⋯	>24.3
LAE 6	24.8	0.22	5.3	26.5	0.31	3.7	1
LAE 7	24.8	0.23	5.2	26.8	0.38	2.8	7.6

Note. [a] In the rest frame.

Table 3
The $z \sim 6.96$ LAE Candidates for the D41 Field

Name	NB973	Error	SNR(NB973)	z'	Error	SNR(z')	EW[a] (Å)
LAE 1	24.6	0.17	7.9	>25.4	⋯	⋯	>24.3
LAE 2	24.7	0.18	7.1	>25.4	⋯	⋯	>24.4
LAE 3	24.8	0.19	6.6	>25.4	⋯	⋯	>24.5
LAE 4	24.9	0.2	6.0	>25.4	⋯	⋯	>24.5
LAE 5	24.9	0.3	5.9	>25.4	⋯	⋯	>24.5
LAE 6	24.9	0.21	5.8	26.7	0.38	2.8	4.4
LAE 7	25.0	0.22	5.6	>25.4	⋯	⋯	>18.4

Note. [a] In the rest frame.

the candidates were Balmer break galaxies, we should have detected them in J with a brighter magnitude in J than in z'.

2. *Extremely red objects (EROs).* We add a criterion to avoid selecting EROs (Cimatti et al. 2002). We constrain this contamination by applying $NB973 - J < 0$, and also by verifying $NB973 - H < 0$ and $NB973 - K_s < 0$.

These red continuum galaxies are therefore generally brighter in the K_s band than in $NB973$. These objects cannot contaminate our candidate samples. However, as our NIR data do not cover our entire fields, we cannot completely rule out this contamination.

3.3.5. False Detections

In order to estimate the number of false detections that could pass our selection criteria, we create an inverse $NB973$ combined image by multiplying this $NB973$ image by -1. We then apply the first criterion used for the candidate selection: SNR($NB973_{\text{combined}}$) $> 5\sigma$. No detection meets this condition. We find therefore that our candidate samples are not contaminated by false detections.

3.4. Summary

After this analysis, we can conclude that it is unlikely that our $z \sim 7$ LAE candidates are contaminated by low-redshift interlopers.

A more detailed study of the foreground emitters (Hα at ~ 0.47, [O III] at ~ 0.95, and [O II] at ~ 1.6) will be presented in a forthcoming paper.

3.5. Final Sample

We obtain a final sample in each observed field. The D33 final sample contains seven $z \sim 7$ LAE candidates over the range of $NB973 = 24.3$–24.8 and SNR($NB973$) $= 5.2$–7.7, and the D41 final sample contains seven $z \sim 7$ LAE candidates in a range of $NB973 = 24.6$–25.0 and SNR($NB973$) $= 5.6$–7.9, as described in Tables 2 and 3 and presented in Figures 3 and 4. Using the equation given below, we estimate the lower limits of the rest-frame equivalent widths derived from the photometric data and report them in Tables 2 and 3. It is interesting to observe that the candidates from the D41 field, which is deeper than the D33 field (see Table 1), are automatically fainter than the D33 ones. The observational conditions for both fields show a systematic difference of at least 0.1 arcsec in seeing:

$$\text{EW}_{\text{rest}} = \left(\frac{f_{NB973} \Delta\lambda_{z'} - f_{z'} \Delta\lambda_{NB973}}{f_{z'} - f_{NB973}} \right) \times \frac{1}{1+z}, \quad (2)$$

where f_{NB973} is the observed flux in the NB combined image, $f_{z'}$ is the observed flux in the z'-broadband image, and $\Delta\lambda_{NB973}$ and $\Delta\lambda_{z'}$ are the widths of the $NB973$ filter (200 Å) and the z'-band filter (928 Å), respectively.

Following Ota et al. (2010), we assume that 77% of the NB flux comes from the Lyα line: $f_{\text{Ly}\alpha} \sim 0.77 f_{NB973}$. We use the detection limit in the z' band to derive in turn lower EW limits.

In the D33 field, LAE 1 has an $NB973$ magnitude corresponding to 94% completeness, and LAE 7 has an $NB973$ magnitude corresponding to 89% completeness. In the D41 field, LAE 1 has an $NB973$ magnitude corresponding to 96% completeness, and LAE 7 has an $NB973$ magnitude corresponding to $\sim 89\%$ completeness. To estimate the completeness, we add 200 artificial star-like objects per bin of 0.1 mag in the blank regions of the stacked images. We then run SExtractor on the image with the same parameters as those previously used for object detection. This procedure is repeated 20 times. The average count on 20 times of the number of artificial stars retrieved in each magnitude bin provides a direct measure of the completeness limit.

4. DISCUSSION

4.1. Variance

Two sources of variance can affect a high-redshift study: the Poisson variance and the cosmic variance; in other words, the fluctuations in the large-scale distribution of the galaxies. In order to estimate the value of this cosmic variance we use the online calculator[7] from the model of Trenti & Stiavelli (2008). We then obtain values of 37% and 36% of cosmic variance in the D33 and D41 fields, respectively.

Considering the limited number of objects in our sample and the large comoving volume of our survey, our results are as limited by Poisson noise ($\sim 38\%$ for the seven objects of the D33 field and for the seven objects of the D41 field) as by clustering. Therefore, in the case in which the full sample in each observed field (seven candidates in each field) is taken into account (see Section 4.2.1), the error bars represent the Poisson variance and the cosmic variance. In the two other cases (see Sections 4.2.2 and 4.2.3), our results are more limited by the Poisson noise than by clustering. The error bars therefore represent the Poisson noise only.

For the D33 field, we obtain a total fractional error on number counts of 0.65. Since we obtain seven objects in D33, we should expect between 4.5 and 9.4 objects in D41, if the field-to-field variation is within 1σ. Since we found seven objects in the D41

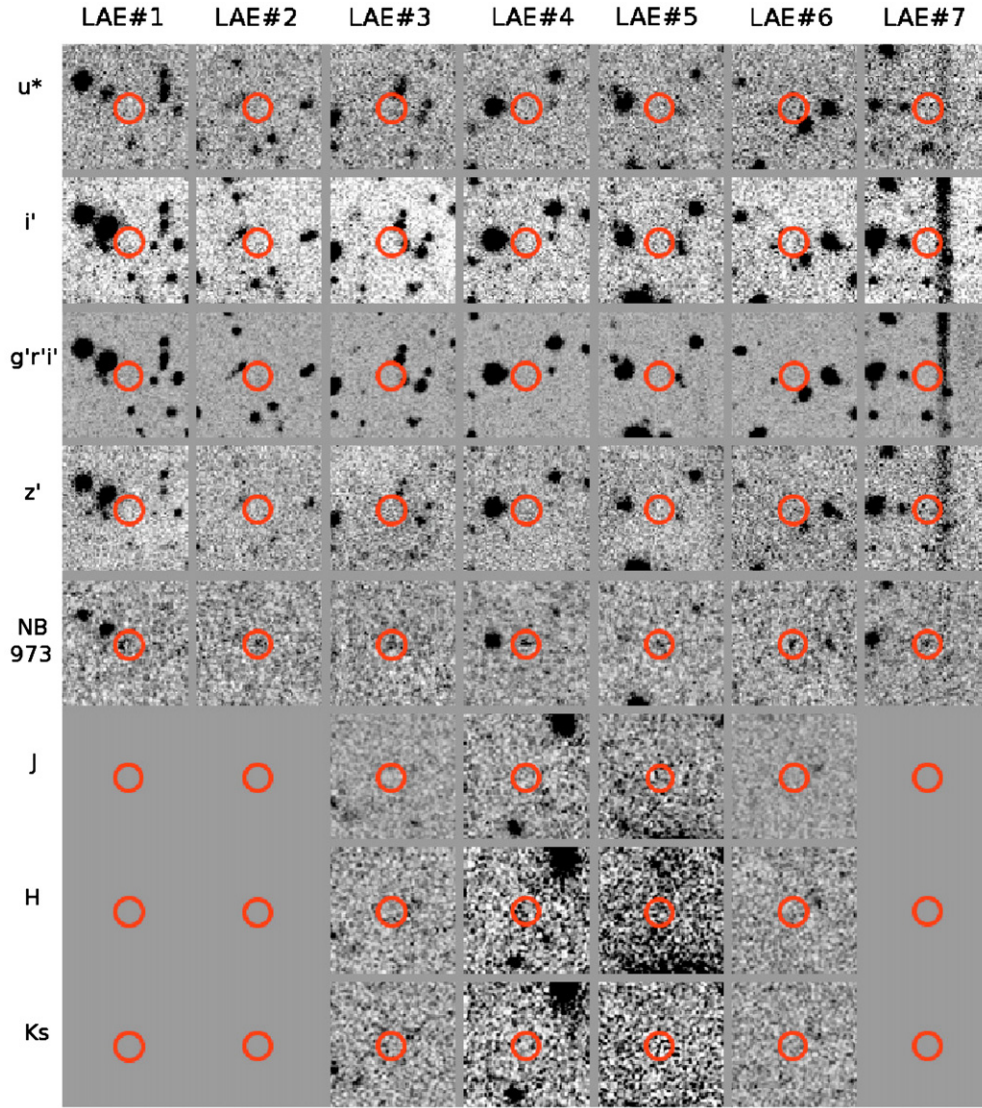7 http://casa.colorado.edu/~trenti/CosmicVariance.html

Figure 3. Thumbnail images of the D33 candidates listed in Table 2. Each window is $15'' \times 15''$. Object names and passbands are located above and to the left of the thumbnails, respectively.

(A color version of this figure is available in the online journal.)

field, we can therefore confirm that the field-to-field variation is within 1σ. This result was expected, as none of our fields are known to be located in overdense or underdense large-scale structure at this redshift.

4.2. Luminosity Function

Following Ota et al. (2010), we assume that on average 77% of the NB flux comes from the Lyα line. We therefore apply the same correction factor during the conversion from $NB973$ to Lyα fluxes.

To the Lyα LF of these $z \sim 7$ LAE samples, we fit a Schechter function, $\Phi(L)$, given by

$$\Phi(L)dL = \Phi^* \left(\frac{L}{L^*} \right)^\alpha \exp \left(-\frac{L}{L^*} \right) \frac{dL}{L^*}, \qquad (3)$$

in order to compare with previous high-redshift works (Hibon et al. 2010; Ouchi et al. 2010, 2008; Ota et al. 2008). The error bars shown in Figure 5 represent the total errors (cumulative Poisson errors and cosmic variance) as explained in Section 4.1.

In the case of Figures 6 and 7, the results are more limited by the Poisson noise than by the cosmic variance. The error bars then represent only the cumulative Poisson errors. Considering the low number of candidates in our sample, we choose to fit two out of three of the Schechter function parameters. Following Hibon et al. (2010) and Ouchi et al. (2008), we set the faint end slope of the luminosity, α, to $\alpha = -1.5$, and determine Φ^* and L^* by χ^2 minimization. We correct the data from the completeness by number weighting.

We decide to study the following different cases:

1. The full sample of each field is real.

2. The samples are contaminated by 50%. We then consider only the four brightest objects of each field as real (later referred to as bright samples). This is justified by the fact that the brightest candidates are the most robust ones, and we are focusing on building the bright end of the $z \sim 7$ Lyα LF.

3. We choose to derive a common Lyα LF for the D33 and D41 LAE brightest candidates. We therefore have a sample of eight bright objects in a total area of 2320 arcmin^2,
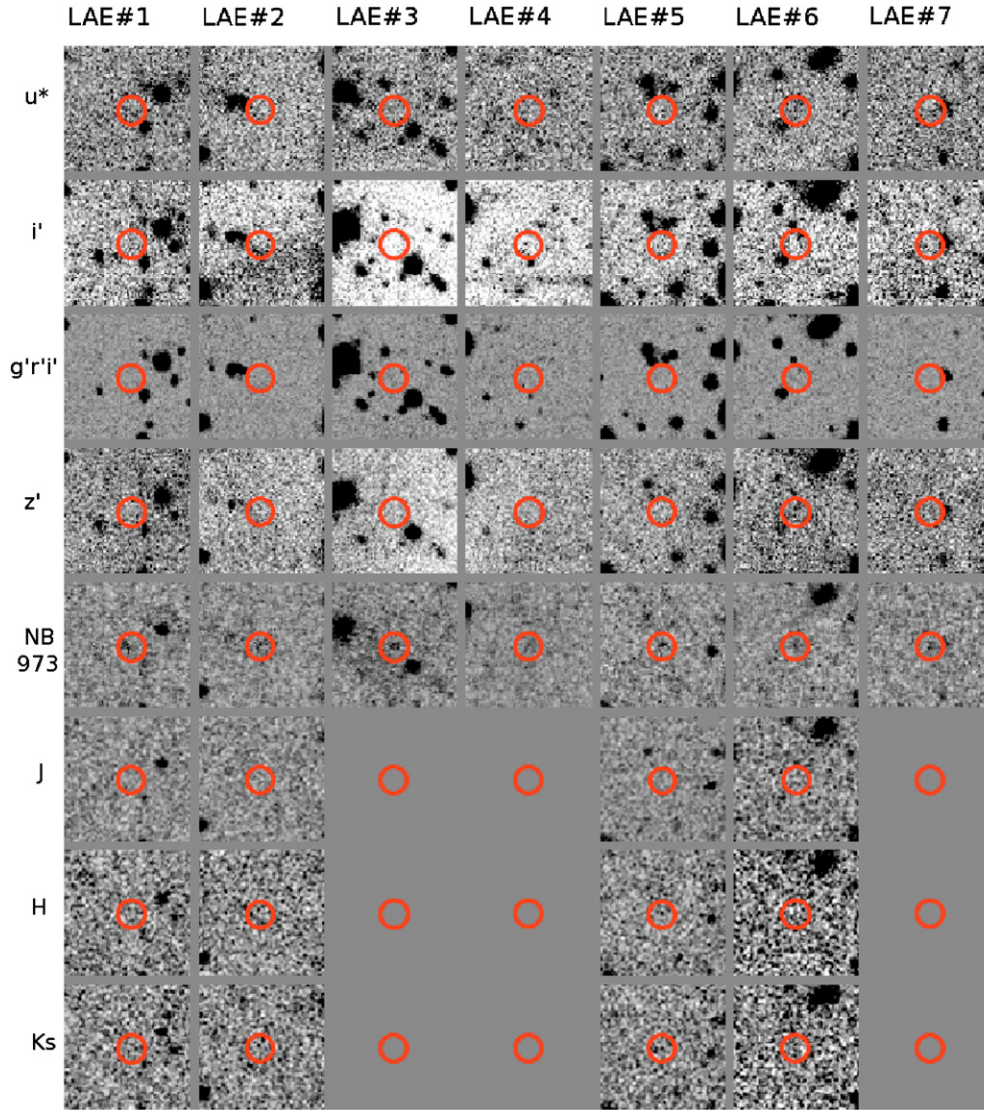
Figure 4. Thumbnail images of the D41 candidates listed in Table 2. Each window is $15'' \times 15''$. Object names and passbands are located above and to the left of the thumbnails, respectively.

(A color version of this figure is available in the online journal.)

corresponding to the sum of the D33 and D41 effective areas.

The best-fit Schechter LF parameters for each case are summarized in Table 4.

4.2.1. All the Candidates are Real

From the $z \sim 7$ Lyα LF derived from the full sample of the D41 field, shown in Figure 5 as the blue line, and the corresponding candidates represented as filled squares, we observe a possible but weak evolution in luminosity from the $z \sim 6.5$ Lyα LF from Ouchi et al. (2010) (dot-long-dashed line in Figure 5), but no possible evolution from the $z \sim 6.5$ Lyα LF from Kashikawa et al. (2011) (dot-short-dashed line in Figure 5). The $z \sim 7$ Lyα LF from the complete sample of the D33 field, shown as the red line and the filled triangles in Figure 5, shows weaker evolution in luminosity from the $z \sim 6.5$ Lyα LF. However, looking at the error bars from the D33 and D41 field candidates, both weak evolutions in luminosity become very discussable. From these possible $z \sim 7$ Lyα LFs,

Table 4
Best-Fit Schechter LF Parameters for $\alpha = -1.5$

Redshift	$\log(L^*(\mathrm{erg\,s^{-1}}))$	$\log(\Phi^*(\mathrm{Mpc^{-3}}))$
$6.96^{(1)}$	$42.50^{+0.1}_{-0.2}$	$-2.40^{+0.15}_{-0.2}$
$6.96^{(2)}$	$42.53^{+0.1}_{-0.2}$	$-2.15^{+0.1}_{-0.1}$
$6.96^{(3)}$	$42.73^{+0.1}_{-0.2}$	$-3.17^{+0.15}_{-0.2}$
$6.96^{(4)}$	$42.56^{+0.1}_{-0.2}$	$-2.73^{+0.1}_{-0.1}$
$6.96^{(5)}$	$43.71^{+0.1}_{-0.1}$	$-3.33^{+0.1}_{-0.1}$
$6.96^{(6)}$	$42.8^{+0.12}_{-0.14}$	$-3.44^{+0.20}_{-0.16}$
$6.5^{(7)}$	$42.64^{+0.1}_{-0.1}$	$-3.07^{+0.13}_{-0.13}$
$5.7^{(8)}$	$42.8^{+0.16}_{-0.16}$	$-3.11^{+0.29}_{-0.31}$

References.
(1) and (2) derived from our D33 and D41 full samples, respectively; (3) and (4) derived from the brightest candidates in each field; (5) derived from a common sample between D33 and D41 fields; (6) Ota et al. 2008; (7) Ouchi et al. 2010; (8) Ouchi et al. 2008.
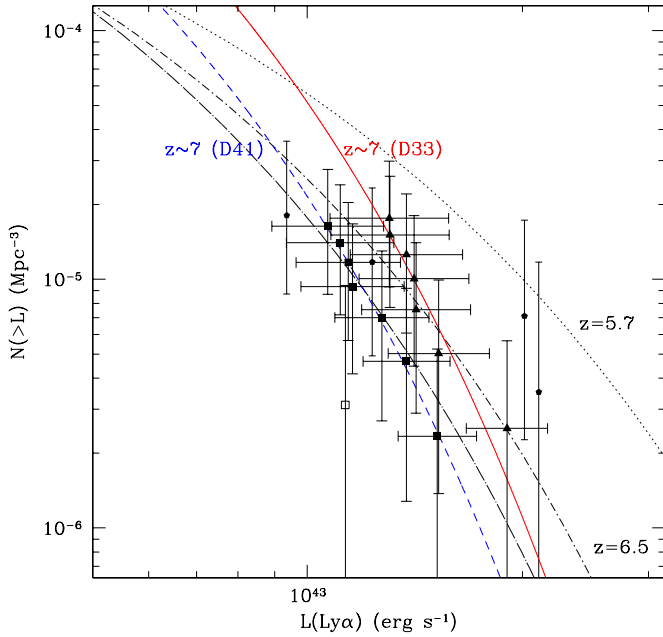
Figure 5. Best-fit Schechter function for the cumulative $z \sim 7$ Lyα luminosity function derived from the D33 full sample (solid line; red in the online journal) and from the D41 full sample (dashed line; blue in the online journal). Our D33 candidates are represented as triangles and the D41 ones as filled squares; the $z = 6.96$ LAE from Iye et al. (2006) is the empty square, and Ota et al. (2010) candidates are pentagons. Also represented here are the $z = 6.5$ Lyα LF from Kashikawa et al. (2011) (dot-short-dashed line), the $z = 6.5$ Lyα LF from Ouchi et al. (2010) (dot-long-dashed line), and the $z = 5.7$ Lyα LF from Kashikawa et al. (2011) (dotted line). The cumulative Poisson errors and the cosmic variance are taken into account in the vertical error bars.

(A color version of this figure is available in the online journal.)

if all the candidates are real for one of the observed fields, we cannot therefore make a conclusion about possible evolution in luminosity from $z \sim 6.5$ to $z \sim 7$.

4.2.2. Only the Brightest Candidates are Real

We derive Lyα LFs for the two different $z \sim 7$ bright LAE candidate samples. The best-fit Schechter functions are shown in Figure 6. In both cases, we do not observe a significant evolution in either density or in luminosity from $z \sim 6.5$, from Ouchi et al. (2010) or Kashikawa et al. (2011), to $z \sim 7$.

4.2.3. One Common LF for both Fields Bright Sample

By fitting a unique Schechter LF for both samples (as seen in Figure 7), we assume that the brightest objects from both samples are real $z \sim 7$ LAEs. Looking only at the filled triangles in Figure 7, representing the four brightest candidates from D41 and the ones from D33, we remark that they fit the $z \sim 6.5$ Lyα LF from Ouchi et al. (2010) but not the $z \sim 6.5$ Lyα LF from Kashikawa et al. (2011). Depending on the $z \sim 6.5$ Lyα LF we considered, the best-fit Schechter-derived LF, shown as the red line in Figure 7, could agree with the observed evolution between $z \sim 5.7$ and $z \sim 6.5$ but would not be in favor of a strong evolution between $z \sim 6.5$ and $z \sim 7$.

4.2.4. Summary

We obtain two different best-fit Schechter functions for the $z \sim 7$ cumulative LF from our two different sets of photometric candidates. Both candidate samples help in building the bright end of the $z \sim 7$ LF. Although we do not see an evolution between $z \sim 6.5$ and $z \sim 7$ from the D33 candidate sample, the
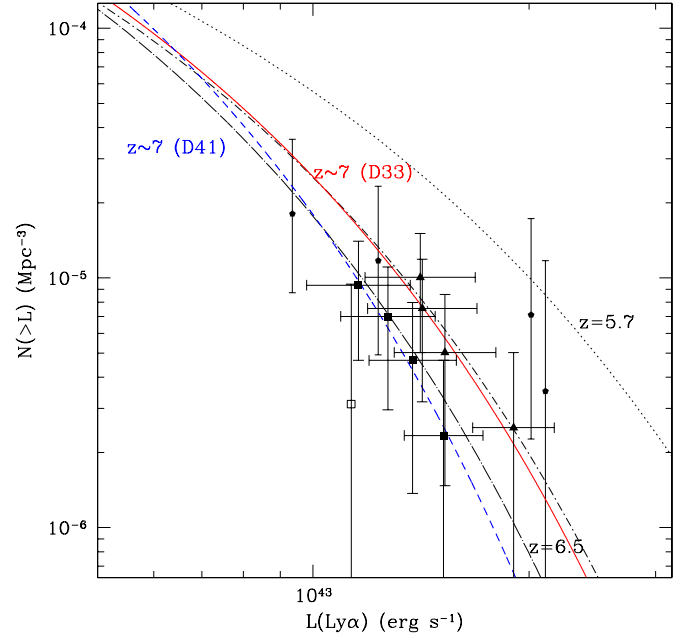

Figure 6. Best-fit Schechter function for the cumulative $z \sim 7$ Lyα luminosity function derived from the D33 bright sample (solid line; red in the online journal) and from the D41 full sample (dashed line; blue in the online journal). Our D33 candidates are represented as triangles and the D41 ones as filled squares; the $z = 6.96$ LAE from Iye et al. (2006) is the empty square. Also represented here are the $z = 6.5$ Lyα LF from Kashikawa et al. (2011) (dot-short-dashed line), the $z = 6.5$ Lyα LF from Ouchi et al. (2010) (dot-long-dashed line), and the $z = 5.7$ Lyα LF from Kashikawa et al. (2011) (dotted line). The vertical error bars represent the cumulative Poisson errors, as the bright samples are more limited by the Poisson noise than by clustering.

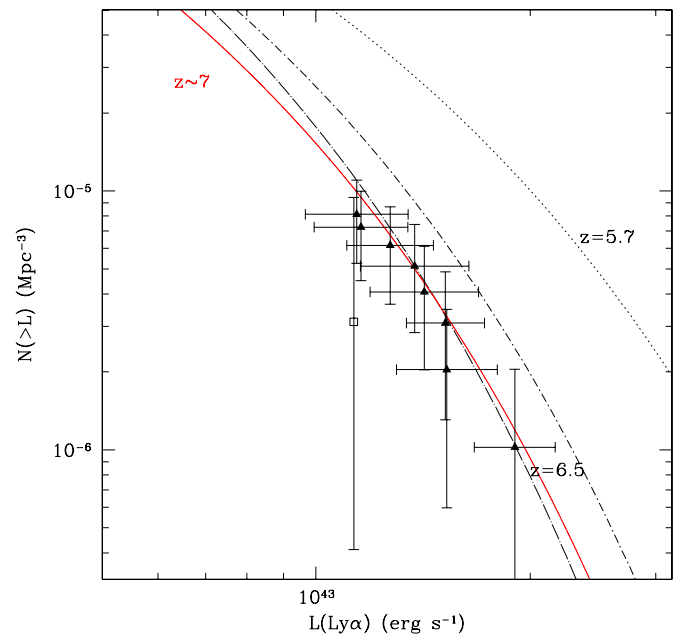(A color version of this figure is available in the online journal.)

Figure 7. Best-fit Schechter function for the cumulative $z \sim 7$ Lyα luminosity function derived from a common sample composed by the D33 bright sample in blue and from the D41 bright sample in red. Our D33 and D41 candidates are represented as triangles; the $z = 6.96$ LAE from Iye et al. (2006) is the empty square. Also represented here are the $z = 6.5$ Lyα LF from Kashikawa et al. (2011) (dot-short-dashed line), the $z = 6.5$ Lyα LF from Ouchi et al. (2010) (dot-long-dashed line), and the $z = 5.7$ Lyα LF from Kashikawa et al. (2011) (dotted line). The vertical error bars represent the cumulative Poisson errors, as the common sample is more limited by the Poisson noise than by clustering.

(A color version of this figure is available in the online journal.)

LF derived from the D41 candidate sample also does not show a significant evolution between $z \sim 6.5$ to $z \sim 7$, as shown in Figure 6.

By producing $z \sim 7$ LF including not only a one-field candidate sample but also the spectroscopically confirmed IOK-1, the best-fit Schechter parameters do change slightly. However, our previous conclusion is still valid.

Assuming that the brightest eight of our candidates are real, we interestingly obtain a $z \sim 7$ LF in agreement with the $z = 6.5$ LF produced by Ouchi et al. (2010).

Ota et al. (2008) presented the first search for $z \sim 7$ LAEs, which has led to the first spectroscopically confirmed $z \sim 7$ LAE. Their imaging survey covers an area of 876 arcmin^2 with the filter $NB973$ ($\Delta\lambda = 200$ Å, $\lambda_c = 9755$ Å) and reaches a 50% completeness of $NB973 = 25.3$ (AB, 3.5σ). IOK-1 has a flux of 2×10^{-17} erg s^{-1} cm^{-2}. We therefore observe a wider but shallower area. This strategy is justified by our willingness to constrain only the bright end of the $z \sim 7$ Lyα LF.

The main prediction of Le Delliou et al. (2006) is a likely moderate decline of the bright end of the LF of LAEs from $z = 6.5$ to $z \sim 7$ arising from the evolution of the mass distribution of dark matter halos. If the LF undergoes limited evolution between $z = 6.5$ and $z = 7$, the effects induced by the incomplete reionization of the IGM may play an important role in the evolution of the observed LF. The faint galaxies may be more easily obscured by neutral regions and could enhance the bright end of the LF.

By assuming that the LAEs and LBGs show a similar evolution history, Ota et al. (2008) inferred that the Lyα LF derived from LAEs evolves as the rest-frame UVLFs obtained from Lyman break galaxies (LBGs). From Yoshida et al. (2006), they estimated a possible $z \sim 7$ Lyα LF with a pure luminosity evolution of $L^*_{z=7} = 0.58\,L^*_{z=5.7}$, with $L^*_{z=5.7} = 1.08.10^{43}$ erg s^{-1} (Shimasaku et al. 2006). This inferred $z \sim 7$ Lyα LF does not agree with our photometric candidate sample. It confirms their idea that if LAEs are strongly related to LBGs, the neutral hydrogen fraction in the IGM is possibly higher at $z \sim 7$ than at $z \sim 5.7$, and this difference can cause the attenuation of Lyα lines of high-redshift LAEs.

If none of our objects are a real $z \sim 7$ LAE, we can then put an upper limit on the $z \sim 7$ Lyα LF, which helps in better constraining these models.

5. CONCLUSIONS

We observed 0.64 deg^2 of the WIRDS/CFHT-LS fields with the $NB973$ filter, targeting the Lyα line at $z \sim 7$. After applying our selection criteria and verifying that our selection was not contaminated by low-redshift emitters, we obtained a sample of seven $z \sim 7$ LAEs in each field. From these photometric samples, we were able to infer possible $z \sim 7$ Lyα LFs. We did not find a

significant evolution in either luminosity or in density from $z = 6.5$ to $z \sim 7$.

It is now crucial to obtain spectroscopic follow-up observations to reveal the real nature of these objects and establish a firm conclusion about the $z \sim 7$ Lyα LF. The exact evolution of the LF beyond redshift 6.5 therefore remains a matter of debate. Moreover, a single galaxy at $z \sim 7$ is obviously not sufficient to firmly constrain the bright end of the Lyα LF. We need to increase the number of independent fields as well as the number of LAEs at $z = 7$. Once the bright end of $z \sim 7$ Lyα LF is determined and possible evolution from $z = 6.5$ is derived, it will become easier to assess whether the 1.06 μm and the 1.19 μm NB filters could reveal $z \sim 8$–9 LAEs.

REFERENCES

Bertin, E., & Arnouts, S. 1996, A&AS, 117, 393
Cappellaro, E., Evans, R., & Turatto, M. 1999, A&A, 351, 459
Cardamone, C., Schawinski, K., Sarzi, M., et al. 2009, MNRAS, 399, 1191
Cimatti, A., Daddi, E., Mignoli, M., et al. 2002, A&A, 381, L68
Daddi, E., Cimatti, A., Renzini, A., et al. 2004, ApJ, 617, 746
Delorme, P., Albert, L., Forveille, T., et al. 2010, A&A, 518, A39
Hawley, S. L., Covey, K. R., Knapp, G. R., et al. 2002, AJ, 123, 3409
Hayashi, M., Kodama, T., Koyama, Y., Tadaki, K.-I., & Tanaka, I. 2011, MNRAS, 415, 2670
Hibon, P., Cuby, J., Willis, J., et al. 2010, A&A, 515, A97
Hibon, P., Malhotra, S., Rhoads, J., & Willott, C. J. 2011, arXiv:1109.009
Hu, E. M., Cowie, L. L., Barger, A. J., et al. 2010, ApJ, 725, 394
Hu, E. M., Cowie, L. L., McMahon, R. G., et al. 2002, ApJ, 568, L75
Iye, M., Ota, K., Kashikawa, N., et al. 2006, Nature, 443, 186
Kashikawa, N., Shimasaku, K., Malkan, M. A., et al. 2006, ApJ, 648, 7
Kashikawa, N., Shimasaku, K., Matsuda, Y., et al. 2011, ApJ, 734, 119
Kulkarni, S. R., & Rau, A. 2006, ApJ, 644, L63
Le Delliou, M., Lacey, C. G., Baugh, C. M., & Morris, S. L. 2006, MNRAS, 365, 712
Malhotra, S., & Rhoads, J. E. 2004, ApJ, 617, L5
McCracken, H. J., Capak, P., Salvato, M., et al. 2010, ApJ, 708, 202
Ota, K., Iye, M., Kashikawa, N., et al. 2008, ApJ, 677, 12
Ota, K., Iye, M., Kashikawa, N., et al. 2010, ApJ, 722, 803
Ouchi, M., Shimasaku, K., Akiyama, M., et al. 2008, ApJS, 176, 301
Ouchi, M., Shimasaku, K., Furusawa, H., et al. 2010, ApJ, 723, 869
Ouchi, M., Shimasaku, K., Okamura, S., et al. 2004, ApJ, 611, 660
Regnault, N., Conley, A., Guy, J., et al. 2009, A&A, 506, 999
Rhoads, J. E., & Malhotra, S. 2001, ApJ, 563, L5
Salzer, J. J., Jangren, A., Gronwall, C., et al. 2005, AJ, 130, 2584
Shimasaku, K., Kashikawa, N., Doi, M., et al. 2006, PASJ, 58, 313
Spergel, D. N., Bean, R., Doré, O., et al. 2007, ApJS, 170, 377
Trenti, M., & Stiavelli, M. 2008, ApJ, 676, 767
Xia, L., Malhotra, S., Rhoads, J., et al. 2011, AJ, 141, 64
Yagi, M., Kashikawa, N., Sekiguchi, M., et al. 2002, AJ, 123, 66
Yoshida, M., Shimasaku, K., Kashikawa, N., et al. 2006, ApJ, 653, 988
Zacharias, N., Urban, S. E., Zacharias, M. I., et al. 2004, AJ, 127, 3043